Acta Oceanol. Sin., 2024, Vol. 43, No. 8, P. 13–25
https://doi.org/10.1007/s13131-023-2274-7
http://www.aosocean.com
E-mail: ocean2@hyxb.org.cn

Tomographic inversion of OBS converted shear waves: case study of profile EW6 in the Dongsha area

Genggeng Wen[1, 2, 3], Kuiyuan Wan[4, 5*], Shaohong Xia[4, 5*], Xiuwei Ye[1, 2, 3], Huilong Xu[4, 5], Chaoyan Fan[4, 5], Jinghe Cao[4, 5], Shunshan Xu[6]

[1] CEA Key Laboratory of Earthquake Monitoring and Disaster Mitigation Technology, Guangdong Earthquake Agency, Guangzhou 510070, China

[2] Guangdong Science and Technology Collaborative Innovation Center for Earthquake Prevention and Disaster Mitigation, Guangzhou 510070, China

[3] MOE Key Laboratory of Disaster Forecast and Control in Engineering-Urban Earthquake Safety Laboratory, Guangzhou 510070, China

[4] CAS Key Laboratory of Ocean and Marginal Sea Geology, South China Sea Institute of Oceanology, Chinese Academy of Sciences, Guangzhou 510301, China

[5] Southern Marine Science and Engineering Guangdong Laboratory (Guangzhou), Guangzhou 511458, China

[6] Centro de Geociencias, Universidad Nacional Autónoma de México, Querétaro, C.P. 76230, Mexico

Received 28 April 2023; accepted 29 September 2023

Abstract

Studies of converted S-wave data recorded on the ocean bottom seismometer (OBS) allow for the estimation of crustal S-wave velocity, from which is further derived the *Vp*/*Vs* ratio to constrain the crustal lithology and geophysical properties. Constructing a precise S-wave velocity model is important for deep structural research, and inversion of converted S-waves provides a potential solution. However, the inversion of the converted S-wave remains a weakness because of the complexity of the seismic ray path and the inconsistent conversion interface. In this study, we introduced two travel time correction methods for the S-wave velocity inversion and imaged different S-wave velocity structures in accordance with the corresponding corrected S-wave phases using seismic data of profile EW6 in the northeastern South China Sea (SCS). The two inversion models show a similar trend in velocities, and the velocity difference is <0.15 km/s (mostly in the range of 0–0.1 km/s), indicating the accuracy of the two travel time correction methods and the reliability of the inversion results. According to simulations of seismic ray tracing based on different models, the velocity of sediments is the primary influencing factor in ray tracing for S-wave phases. If the sedimentary layer has high velocities, the near offset crustal S-wave refractions cannot be traced. In contrast, the ray tracing of Moho S-wave reflections was not significantly impacted by the velocity of the sediments. The two travel time correction methods have their own advantages, and the application of different approaches is based on additional requirements. These works provide an important reference for future improvements in converted S-wave research.

Key words: converted S-wave, S-wave velocity structure, inversion, ocean bottom seismometer, northeastern South China Sea

Citation: Wen Genggeng, Wan Kuiyuan, Xia Shaohong, Ye Xiuwei, Xu Huilong, Fan Chaoyan, Cao Jinghe, Xu Shunshan. 2024. Tomographic inversion of OBS converted shear waves: case study of profile EW6 in the Dongsha area. Acta Oceanologica Sinica, 43(8): 13–25, doi: 10.1007/s13131-023-2274-7

1 Introduction

The ocean bottom seismometer (OBS) deep seismic surveys are a detection technology in which seismic geophones are deployed directly on the seafloor and has become one of the most effective techniques for the study of fine velocity structures of the crust and upper mantle (Zhao et al., 2023; Qi et al., 2021; Xia et al., 2016; Qiu et al., 2011). Ocean bottom seismometer surveys have the advantage of being able to record converted S-wave signals (Xia et al., 2016; Zhao et al., 2007, 2010), and the obtained *Vp*/*Vs* ratios (the ratios of seismic compressional and shear-wave velocities) can provide direct evidence for constraining rock lithology and geophysical properties (Christensen, 1996; Christensen and Mooney, 1995), which has been widely used in studies of crustal lithology (Li et al., 2022; Wen et al., 2021a, 2021b; Zhao et al., 2010; Mjelde et al., 2005; Chian and Louden, 1994), mantle serpentinization (Li et al., 2021; Hou et al., 2019; Grevemeyer et al., 2018), and gas hydrate saturation (Liu et al., 2022; Singhroha et al., 2019; Zhang et al., 2018; Satyavani et al.,

Foundation item: The National Natural Science Foundation of China under contract Nos 42276062 and 42006071; the Seismological Research Foundation for Youths of Guangdong Earthquake Agency under contract No. GDDZY202307; the Strategic Priority Research Program of Chinese Academy of Sciences under contract No. XDA22020303; the Science and Technology Planning Project of Guangdong Province-Guangdong Collaborative Innovation Center for Earthquake Prevention and Disaster Mitigation Technology under contract No. 2018B020207011.

*Corresponding author, E-mail: kywan@scsio.ac.cn; shxia@scsio.ac.cn

2016).

The *RayInvr* forward method (Zelt and Smith, 1992) is extensively applied to obtain S-wave velocity (*Vs*) and *Vp*/*Vs*, which contributed to constrain the properties of the sediments, crust, and mantle (Hou et al., 2019; Wei et al., 2011, 2015, 2017; Zhao et al., 2010; Mjelde et al., 2003, 2005; Digranes et al., 1998; Kodaira et al., 1996; Mjelde, 1992). However, the forward S-wave modeling is severely limited by the geometry of the existing P-wave model, and the Poisson's ratio within one layer can only be set as a single value from top to bottom, resulting in low vertical resolution and sudden horizontal changes in the *Vs* and *Vp*/*Vs* models. Although Zhang et al. (2022) proposed a *RayInvr*-based software tool to avoid abrupt changes in the *Vs* model, the disadvantage of the forward modeling approach is that it does not allow for the application of uncertainty tests, which restricts the interpretation of the results because the *Vp*/*Vs* of different crustal compositions vary within 0.2 (Christensen, 1996).

A better strategy for constructing *Vs* model is to use the tomographic inversion method, which provides a more objective, robust, and detailed model. The ray path of the converted S-wave arrivals when the S-wave originates from sedimentary basement conversion includes both P-wave and *Vs* segments, which makes it difficult to invert the *Vs* because there is no travel time inversion method for the joint inversion of P-wave and S-wave velocities. The current solution is to create "symmetric" seismic waves by correcting the S-wave arrivals' travel times, which are always converted at the same interface when propagating both upward and below. An effective travel time correction method is to make the velocity model have P-wave velocity (*Vp*) above the conversion interface and *Vs* below (double conversion at the interface), which is corrected by calculating the travel time delay between the P-wave arrivals and the corresponding converted S-wave arrivals (Li et al., 2021, 2022; Eccles et al., 2009, 2011; Eccles, 2008). However, it is challenging to estimate the time correction in the case of complicated sedimentary structures, such as the presence of Mesozoic sedimentary layers (Fig. 1) in the northeastern South China Sea (SCS) (Fan et al., 2022; Yan et al., 2014; Hao et al., 2009; Ruan et al., 2009; Shao et al., 2007), because there may be more than one conversion interface (Liu et al., 2023; Wen et al., 2021b; Hou et al., 2019; Wei et al., 2011). In this case, another travel time correction method based on the known sediment velocity and *Vp*/*Vs* is proposed (Wen et al., 2021a, 2021b; Eccles, 2008), making the entire model as an *Vs*. Using the two travel time correction methods described above, the inversion of *Vs* has been successfully completed in the North Atlantic margins (Eccles et al., 2009, 2011), Zhongsha Block (Li et al., 2021, 2022), Dongsha area (Wen et al., 2021b), and Tainan basin (Liu et al., 2023), providing new evidence for revealing the formation mechanism and tectonic evolution of the continental margin. However, the comparison of the results of different travel time correction methods has not been studied.

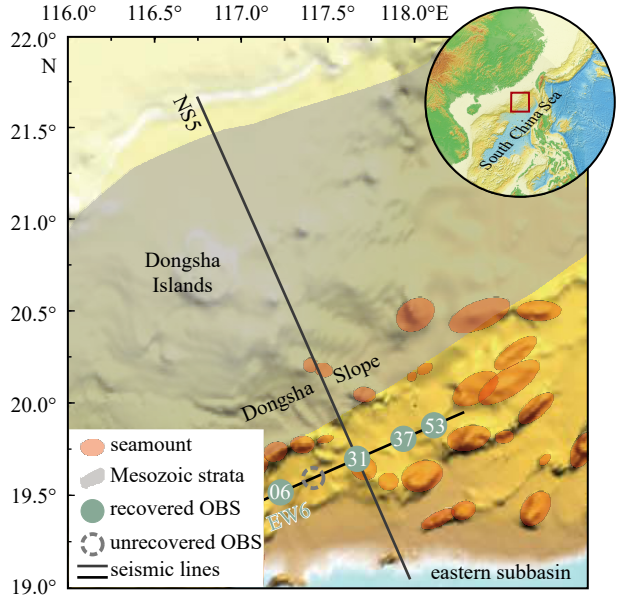

Fig. 1. The OBSs position and seismic survey lines. Gray areas show the distribution of Mesozoic strata in the northeastern SCS (Yang et al., 2015). Red ellipses indicate volcanic seamounts (Fan et al., 2017).

In this study, we applied seismic tomography (Korenaga et al., 2000) to obtain the *Vs* model along the Dongsha area in the SCS (Fig. 1), based on the corrected S-wave arrivals from two travel time correction methods. We assessed the results of the two methods, discussed their advantages and applicability, and analyzed the influences of the sedimentary layer on ray tracing for S-wave phases.

2 Geological setting

The SCS is one of the largest marginal seas in the Western Pacific and is located at the intersection of the Eurasian, India-Australia, and Philippine Sea plates. The SCS has undergone a complete Wilson cycle, including Mesozoic plate subduction, Cenozoic continental rifting, seafloor spreading, and subduction of the present oceanic lithosphere (Sibuet et al., 2016; Lester et al., 2014; Shi and Li, 2012; Li and Li, 2007). The northern SCS is a typical rifting margin and an important tectonic transition zone from the late Mesozoic subduction to the Cenozoic rifting, which not only has recorded the structural information of Mesozoic subduction but also preserved the geological landscape of rifting processes. The distinctive crustal structure of the northern SCS margin is the result of the complicated tectonic setting there. The crustal thickness gradually thinned towards the oceanic basin, from a thickness of 25 km at the continental shelf to 8–12 km near the continent-ocean boundary (Fan et al., 2019; Wan et al., 2019; Xia et al., 2018; Wei et al., 2011; Wang et al., 2006; Yan et al., 2001). The highly extended continental crust beneath the lower continental slope is less than 15 km thick and composed of faulted blocks (Gao et al., 2015) interspersed with volcanic bodies (Lester et al., 2014; Wang et al., 2006; Yan et al., 2001; Nissen et al., 1995). In addition, the high-velocity lower crust (HVLC), which was mostly attributed to post-rift magmatism, was identified in the lowermost crust of the northeastern SCS with a *Vp* of 7.0–7.5 km/s (Wen et al., 2021b; Fan et al., 2019; Wan et al., 2017, 2019; Xia et al., 2018; Zhao et al., 2010; Yan et al., 2001; Nissen et al., 1995). According to the crustal velocity structure obtained in the northeastern SCS, the crust below the lower continental slope has a *Vp* of 5.0–7.5 km/s (Fan et al., 2019; Wan et al., 2019; Wei et al., 2011; Wang et al., 2006) and an *Vs* of 3.0–4.4 km/s (Wen et al., 2021a; Hou et al., 2019; Wei et al., 2011; Zhao et al., 2010). The crustal *Vp*/*Vs* ratio mainly ranges from 1.73 to 1.81, and the relatively high *Vp*/*Vs* (>1.80) in the local area was caused by magmatic intrusion (Liu et al., 2023; Wen et al., 2021b).

3 Data acquisition, processing, and P-wave velocity model

Seismic profile EW6 was collected by RV *Shiyan 2* of the South China Sea Institute of Oceanology (SCSIO), which is a NE-SW oriented line located on the lower continental slope (Fig. 1). The

line is 141.36 km long, and five OBS (four of which were recovered) were deployed at an interval of 20–30 km. The lack of Mesozoic strata beneath the profile EW6 makes it a perfect case study for researching two travel time correction methods. The seismic source consisted of four bolt airguns with a total volume of 6 000 in^3. Along the profile, 420 shots at intervals of 250–300 m were fired. Clear P-wave and S-wave signals were recorded using OBSs. The original OBS data were processed following correction of clock drifts and positions, data format conversion, and band-pass Butterworth filtering (3–10 Hz) (Xia et al., 2007; Zhao et al., 2004). The converted S-wave was mainly recorded in the horizontal components, and the energy was concentrated in the in-line direction. Therefore, we used the energy-scanning method (Zhang et al., 2016) to determine the polarization angle and rotate the two horizontal components into radial (R) and transverse (T) components.

The forward *Vp* model of profile EW6 (Fig. 2a) constructed by Fan et al. (2019) suggested the velocities of sediments and crust

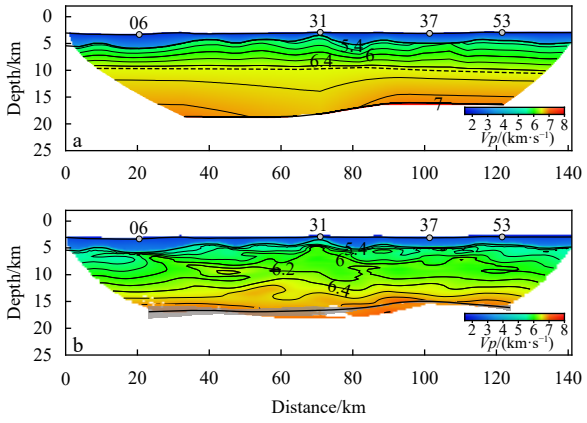

Fig. 2. P-wave velocity model along profile EW6. a. The result of the *RayInvr* forward method (Fan et al., 2019). b. Results of the Tomo2d inversion method. Gray areas show the Moho depth standard deviation. Contour interval is 0.2 km/s.

were 1.7–3.5 km/s and 5.5–7.0 km/s, respectively. The boundary of the upper and lower crust was the 6.5 km/s *Vp* contour in the model. Additionally, we acquired an average tomographic inversion *Vp* model (Fig. 2b) using the phases selected by Fan et al. (2019). The 100 initial models are generated randomly by crustal velocities (5.0–5.5 km/s to 6.8–7.5 km/s) and Moho depth (15–19 km). The forward and inversion models exhibit some differences in crustal velocities due to different modeling methods, but both reveal the absence of HVLC.

4 Identification of S-wave phase and forward modeling

4.1 *Analysis of converted S-wave phase and conversion interface*

The S-wave signals recorded by the OBS originate from P-waves converted to S-waves at the conversion interface. The converted S-wave was classified into PPS and PSS modes (Kodaira et al., 1996). The PPS arrivals are produced by the P-waves converted to an S-wave at an interface on the way up, whereas the PSS arrivals are converted on the way down (Fig. 3). The PPS arrivals have relatively high apparent velocities that are close to the corresponding P-wave arrivals because the ray path of the PPS arrivals is mostly at P-wave velocities. In contrast, the apparent velocities of PSS arrivals were much slower. The conversion modes of the S-waves can be determined by their travel times and apparent velocities.

Identifying the conversion interface is critical for *Vs* modeling since incorrectly determining the interface will lead to significant velocity errors. Generally, P-waves are more likely to convert to S-waves at the interfaces of the seafloor, sedimentary basement, and crust-mantle boundary (Digranes et al., 1998). In our *Vp* model (Fig. 2a), the velocity at the bottom of the sedimentary layer is 3.5 km/s, significantly lower than that at the top of the crust (5.5 km/s). Therefore, conversion is likely to occur at the sedimentary basement. Previous studies revealed that the *Vp/Vs* of Cenozoic sediments in the northeastern SCS was >2 and increased oceanward (Wen et al., 2021b; Hou et al., 2019; Wei et al., 2011), indicating weak sediment consolidation. Conversion may not be expected at the seafloor interface if the sediments are un-

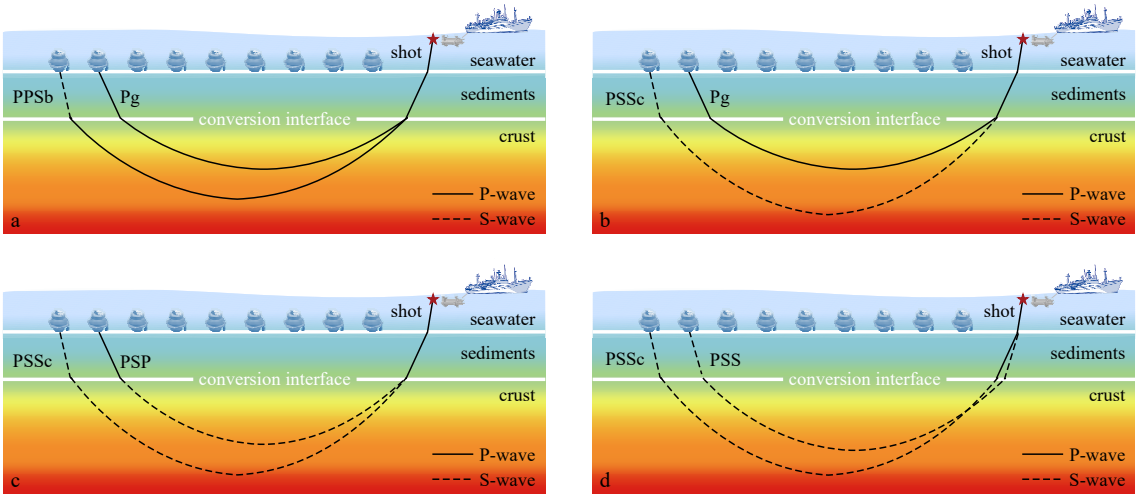

Fig. 3. Schematic diagram of the propagation and conversion of the seismic waves. The PPS arrivals (PPSb) were converted from P-wave to S-wave at an interface on the way up (a), while the PSS arrivals (PPSc) were converted on the way down (b). The PSP phase (c) is generated from double conversion at an interface, and only as an S-wave through the crust. The PSP converted at the basement once more than the PPSc when the ray was upgoing, whereas the PPSc was still traveling as an S-wave in the sediments until arriving at the OBS. The PSS phase (d) is converted on the way down at the seafloor. The PSS propagates downward in the sediment as an S-wave, while PPSc is a P-wave.

consolidated (Li et al., 2022). We thereby infer that the conversion interface is probably the sedimentary basement rather than the seafloor because the OBS was deployed on the lower continental slope, which has a high *Vp/Vs* in sediment.

To further determine the conversion interface, Zoeppritz's equation (Schoenberg and Protazio, 1992) was used to estimate the transmission coefficient for P-wave conversion to S-wave at the interface. The possible partitioning of P-wave and S-wave energies at the interface was calculated based on the different models (Fig. 4). The *Vs* of the uppermost sediments was estimated by Scholte-wave dispersion analysis to be <0.3 km/s (Wang et al., 2022; Du et al., 2020), which was applied in sediment models (Fig. 4a). The density parameters of each layer in the model were obtained from Fan et al. (2019). All the converted S-wave phases in this study can be regarded as transmitted S-waves because the seismic phases were propagated through the conversion interface. In Fig. 4, the transmission coefficient values (St) for an incident P-wave converting to an S-wave at the sedimentary basement interface are 0.29–0.61 within the range of the effective incidence angle, which is greater than that of the seafloor interface (0.02–0.12). Our results further confirm that the conversion occurred at the sedimentary basement interface.

4.2 *Forward S-wave model*

Forward *Vs* modeling was performed using the *RayInvr* forward method (Zelt and Smith, 1992). During the modeling procedure, the interface of the *Vs* model was kept consistent with the forward *Vp* (Fig. 2a), the interface depths were fixed, and only the Poisson's ratio (σ) of the blocks for each layer was modified to adjust the S-wave velocities. The various Poisson's ratios were tested until the best agreement was obtained between the calculated and observed travel times, and the *Vp/Vs* ratio was calculated using the equation of $\frac{Vp}{Vs}=\sqrt{1+\frac{1}{1-2\sigma}}$.

The PPSb phase was refracted as a P-wave through the crust and converted into an S-wave at the sedimentary basement on the way up. In combination with the analysis of P-wave arrivals, the propagation time delay in the entire sediments between the velocities of the P-wave and S-wave is determined, and the *Vp/Vs* of the sediments beneath the OBS is constrained. It is crucial to note that the obtained *Vp/Vs* of the sediments represent the average *Vp/Vs* of the full sediment column beneath each OBS and not a value for the specific layer, or that the *Vp/Vs* structure varies with depth at each OBS station. The PPSb phase was identified at four OBS stations with an offset of >70 km (Figs 5a and 6a). A total of 522 PPSb phases were fitted, and the RMS misfit was 23–64 ms (for details, see Table 1). Notably, the interpolation from adjacent OBS stations yields the average *Vp/Vs* of the sediment between the two OBS, as the PSSb phase can only determine the *Vp/Vs* of the sediment in an extremely limited area below the OBS (Figs 5c and 6c).

PSS arrivals were extremely important in estimating the crustal *Vp/Vs* ratio because their ray path through the crust was at S-wave velocities. The identified PSS arrivals included the PSSc and PSSmb phases (Figs 5a and 6a). The PSSc phase originated from the P-wave converted to an S-wave at the basement on the way down and refracted as the S-wave through the crust, whereas the PSSmb phase has the same conversion but is reflected at the Moho interface. The PSSc phase was identified with an offset of <60 km and a propagation depth of <15 km (Figs 5d and 6d). The PSSmb phase provided wider coverage because of its reflection from the Moho interface (Figs 5d and 6d). We fitted 370 PSSc and 361 PSSmb phases, and the RMS misfit ranged from 143 ms to 204 ms (for details, see Table 1).

The forward modeling results (Fig. 7) show that the sedimentary layer has a low *Vs* of 0.24–1.10 km/s. The average *Vp/Vs* of the sediments below OBS06, OBS31, OBS37, and OBS53 are 2.80, 7.14, 3.20, and 3.91, respectively. The *Vs* and *Vp/Vs* of the upper crust are 3.0–3.6 km/s and 1.70–1.84. Some regions in the upper crust exhibit *Vp/Vs* of >1.80, which may be caused by magmatic intrusions. However, finer imaging of anomalies cannot be acquired owing to the limited resolution of the modeling methods, which prevents further interpretation of these regions. The *Vs* and *Vp/Vs* in the lower crust range of 3.7–4.0 km/s and 1.70–1.77, respectively.

5 Tomographic inversion of the S-wave model

The ray path of the converted S-wave included both P-wave and S-wave velocity segments. However, the existing 2D velocity modeling method does not allow joint inversion of P-wave and S-wave arrivals. Ray path correction provides a solution for performing seismic tomography of PSS arrivals, which is achieved by correcting travel times. The following two travel time correction methods are introduced.

Method 1 was corrected to PSP′ arrival (Li et al., 2021; Eccles et al., 2009). The propagation time delay in the sediments between the velocities of the P-wave and S-wave (Fig. 3c) is represented by the time difference between the crustal refracted phase (T_{Pg}) and the PPS arrivals (T_{PPSb}). This time delay is approximately equal to the time difference between the PSS arrivals

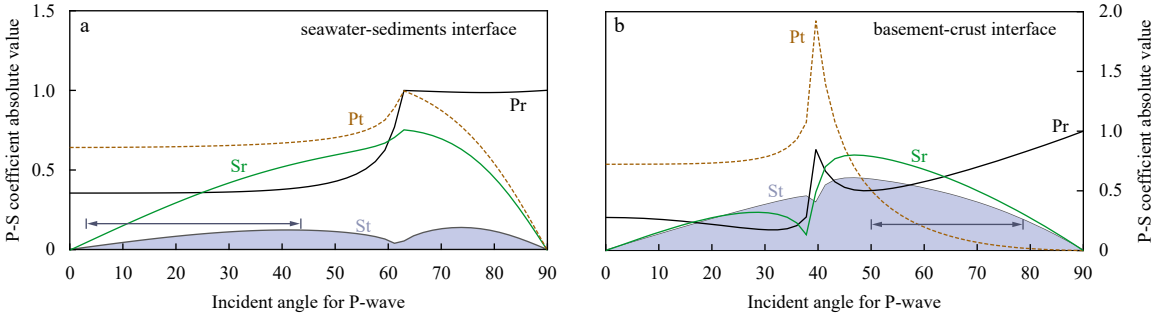

Fig. 4. P-S conversion coefficient absolute value of downward seismic wave in different models. Pr, Pt, Sr, and St represent the reflected and transmitted P-wave and S-wave, respectively. a. model of seawater and the unconsolidated sediments. Vp_1 = 1.5 km/s, Vp_2 = 1.7 km/s, Vs_1 = 0 km/s, Vs_2 = 0.3 km/s, ρ_1 = 1.03 kg/m^3 and ρ_2 =1.92 kg/m^3. b. Model of Cenozoic sediments and crust. Vp_1 = 3.5 km/s, Vp_2 = 5.5 km/s, Vs_1 = 1.3 km/s, Vs_2 = 3.14 km/s, ρ_1 = 2.4 kg/m^3 and ρ_2 = 2.7 kg/m^3. The highly probable range of incident angles (calculated from Snell's Law) for different model are indicated by the arrow.

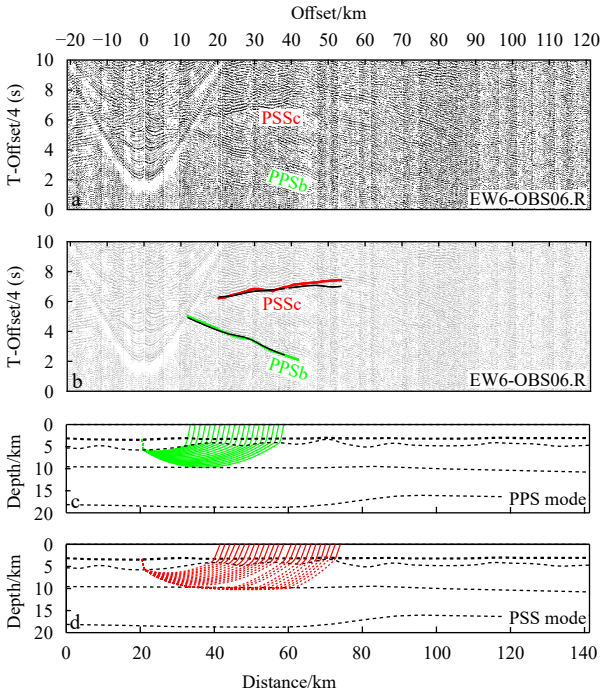

Fig. 5. Seismic profile of radial component at OBS06, with the reduced velocity of 4 km/s (a). The colored dashed lines represent picked travel times, and the thin black lines represent calculated travel times (b). c and d show the ray tracing of PPS and PSS conversion modes, respectively. Solid lines represent P-wave paths, and dotted lines represent S-wave paths.

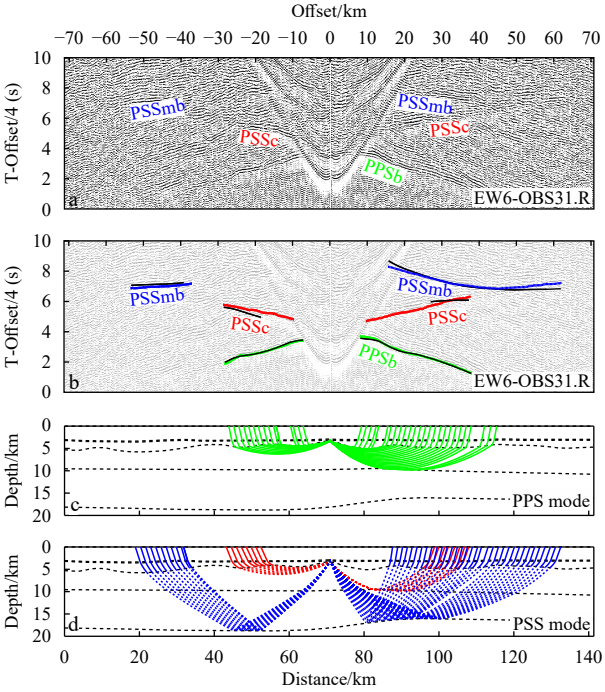

Fig. 6. Seismic profile of radial component at OBS31, with the reduced velocity of 4 km/s (a). The colored dashed lines represent picked travel times, and the thin black lines represent calculated travel times (b). c and d show the ray tracing of PPS and PSS conversion modes, respectively. Solid lines represent P-wave paths, and dotted lines represent S-wave paths.

Table 1. Travel time simulation results for different converted S-wave phases from forward modeling

Station	Mode	Phase	Number of picks	Picking uncertainty/s	RMS/s	χ^2	Conversion interface
06	PPS	PPSb	80	0.12	0.061	0.263	Basement
	PSS	PPSc	99	0.16	0.198	2.012	Basement
31	PPS	PPSb	166	0.10	0.064	0.413	Basement
	PSS	PSSc	62	0.18	0.204	0.648	Basement
		PSSmb	178	0.18	0.168	0.885	Basement
37	PPS	PPSb	178	0.10	0.023	0.055	Basement
	PSS	PSSc	145	0.14	0.185	1.761	Basement
		PSSmb	63	0.16	0.165	1.081	Basement
53	PPS	PPSb	98	0.10	0.031	0.100	Basement
	PSS	PSSc	64	0.14	0.143	1.056	Basement
		PSSmb	120	0.18	0.182	1.035	Basement

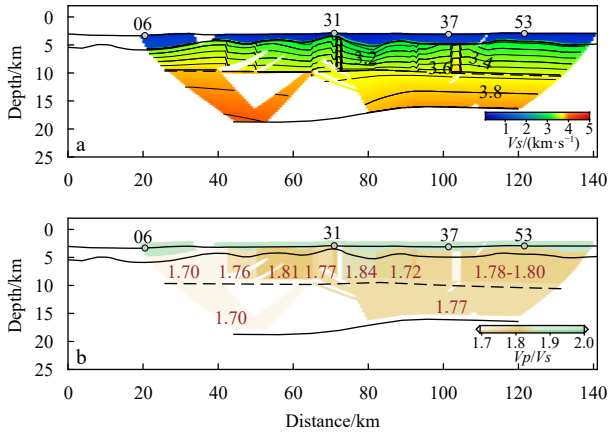

Fig. 7. The *Vs* model from *RayInvr* forward method. The contour interval is 0.1 km/s (a). *Vp/Vs* model (b). The red numbers in the model represent the *Vp/Vs* ratio.

(T_{PSSc}) and double basement conversion arrivals (T_{PSP}). Based on the above analysis, the *PSS* arrivals can be corrected to PSP′ arrivals (PSP′ and PSmP′ phases) (Figs 8 and 9) according to the equation of $T_{\mathrm{PSP'}} = T_{\mathrm{PSS}} - \left(T_{\mathrm{PPSb}} - T_{\mathrm{Pg}}\right)$. This correction makes ray paths have P-wave velocities above the basement and S-wave velocities below.

Method 2 was corrected to PSS′ arrivals (Wen et al., 2021a; Eccles, 2008). *RayInvr* allows flexibility in modeling different arrivals and conversions (Eccles et al., 2009). Based on the *Vs* structures of the sediments obtained from forward modeling (Fig. 7a), the theoretical time delay (T_{S}-T_{P}) between the basement conversion arrivals and seafloor conversion arrivals was calculated (Fig. 3d). Thus, the PSS arrivals (PSSc and PSSm) can be corrected to PSS′ arrivals (PSS′ and PSSm′ phases) (Figs 8 and 9). The entire path through the model is at S-wave velocities because the conversion interface of the PSS arrivals is corrected from the basement to the seafloor.

To avoid additional time errors introduced by the variation in sediment velocities during the inversion procedure, the sediment velocities must be fixed. Therefore, variable velocity damping was applied to the sediment and crust. The velocity damping weight was 10 000 above the basement to hold the sediment velocities fixed and 10 below the basement. Moho depth was inherited from the P-wave inversion model (Fig. 2b). A depth damping weight of 1 000 was chosen to ensure that the Moho depth was fixed owing to the limited coverage of the S-wave reflections. To

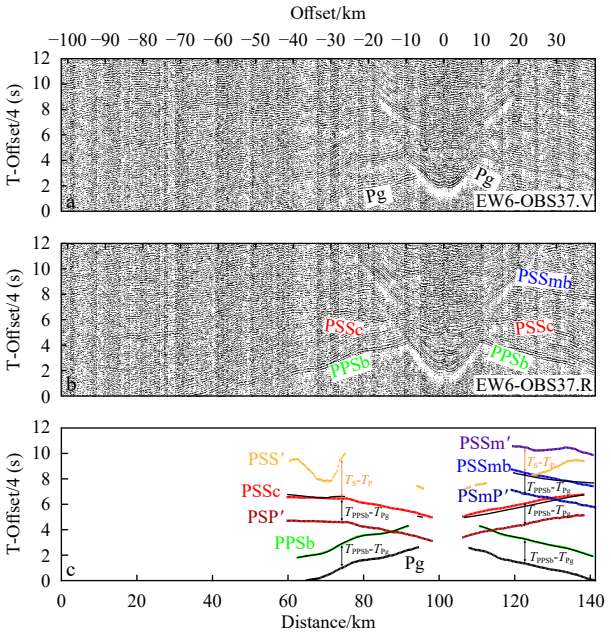

Fig. 8. Travel time corrections of converted S-wave phases recorded by OBS37. a and b are seismic profiles of vertical and radial components, respectively, with a reduced velocity of 4 km/s. c. show the identification and travel time correction of S-wave phases; colored lines represent picked travel times (PSSm′, PSS′, PSP′, and PSmP′ are corrected travel times), and the thin black lines represent calculated travel times from forward modeling.

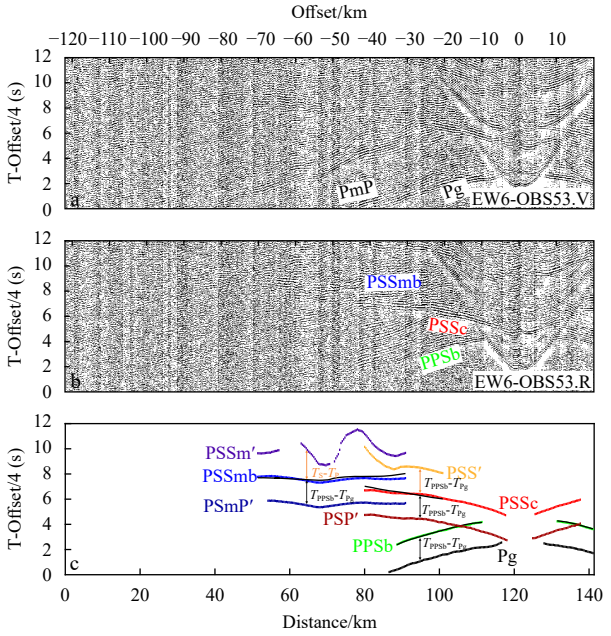

Fig. 9. Travel time corrections of converted S-wave phases recorded by OBS53. a and b are seismic profiles of vertical and radial components, respectively, with a reduced velocity of 4 km/s. c. shows the identification and travel time correction of S-wave phases, colored lines represent picked travel times (PSSm′, PSS′, PSP′, and PSmP′ are corrected travel times), and the thin black lines represent calculated travel times from forward modeling.

make the inversion models based on the two correction methods comparable, other parameters of the two inversions should be consistent. The horizontal grid size is set to 0.5 km, and the vertical grid size is 0.05 km and increases to 0.25 km at 20 km depth. The horizontal and vertical correlation lengths are defined as 1–4 km and 0.1–0.4 km from the top to the bottom, respectively. The smoothing weights of the velocity and depth are set to 100 and 10, respectively. The correlation length of the Moho reflector is set to 6 km, and the depth kernel weighting parameter is set to 1.

5.1 *Inversion model based on PSP′ arrivals*

The PSP′ arrivals have P-wave velocities in the sediments and S-wave velocities in the crust; therefore, the sediment velocities of the initial *Vs* model come from the *Vp* model (Fig. 2b). In the P-wave inversion, the initial crustal velocities were set to be 5.0–5.5 km/s and 6.8–7.5 km/s at the top and bottom, respectively. We thereby set the initial crustal S-wave velocities from 2.78–3.24 km/s to 3.78–4.41 km/s based on the results that the *Vp/Vs* of the crust in the northeast SCS is mostly in the range of 1.70–1.80 (Wen et al., 2021b; Hou et al., 2019; Wei et al., 2011; Zhao et al., 2010). Based on the crustal S-wave velocities described above, we generated 100 randomized initial models. The target chi-square value (χ^2) was set to 1.2, the maximum number of iterations was set to 6, and 100 models were inverted. We obtained 97 inversion results with good convergence, and each model fit the 368 PSmP′ phases. The RMS misfit converged to 131–181 ms, and the χ^2 was 0.677–1.186. Finally, the average tomographic Vs, standard deviation, and *Vp/Vs* models were obtained (Fig. 10).

The results suggest that the crust has a *Vs* of 3.0–4.0 km/s, which does not represent a large-scale HVLC. Beneath the model distance of 100 km, the velocity contours at the bottom of the crust were slightly raised, which could be caused by magmatic intrusions (Fig. 10a). The velocity standard deviation in the sediments was <0.03 km/s, indicating that the velocities were fixed and the expected inversion requirements were completed. The crust has a standard deviation of <0.09 km/s, suggesting that the velocity model is relatively stable (Fig. 10b). Crustal *Vp/Vs* ratios derived from the inversion model were mostly in the range of 1.70–1.94 (Fig. 10c). High *Vp/Vs* (>1.80) were found in the shallow crust. Considering the large degree of crustal extension in the study area, we infer that the high *Vp/Vs* are related to the faults and intruded volcanic bodies.

5.2 *Inversion model based on PSS′ arrivals*

The PSS′ arrivals are obtained based on the original arrivals and the calculated propagation time delay in the sediments at the velocities of P-wave and S-wave. We performed a ray tracing experiment using the initial and corrected arrivals to evaluate the influence of travel time correction on the ray paths through the crust. The forward crustal S-wave velocity model was employed here (Fig. 7a). The ray tracing results indicated that the corrected ray paths through the crust were almost consistent with the original ray paths, with a distance difference of <1 km (Fig. 11). This error is acceptable when the model resolution is considered. In addition, the RMS misfit between the initial and corrected arrivals is mainly within 20 ms (for details, see Table 2), indicating that the results of the travel time correction are accurate.

The ray path of the PSS′ arrivals is at S-wave velocities below the seafloor. Hence, the initial sediment model comes from the forward *Vs* model (Fig. 7a). One hundred initial crustal models are also randomly produced at velocities ranging from 2.78–3.24 km/s to 3.78–4.41 km/s, and the models are inverted using

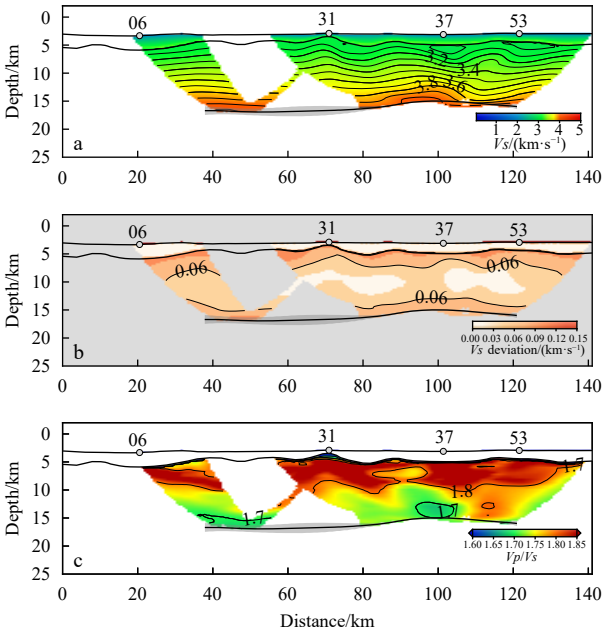

Fig. 10. Final tomographic *Vs* model based on PSP′ phases. a. The average *Vs* model. The contour interval is 0.1 km/s. The velocity value that corresponds to the color scale in the sediment represents the *Vp*. b. The standard deviation of *Vs*. c. The *Vp/Vs* model calculated from the division of the *Vp* (Fig. 2b) and *Vs* models (Fig. 10a). Gray areas show the Moho depth standard deviation.

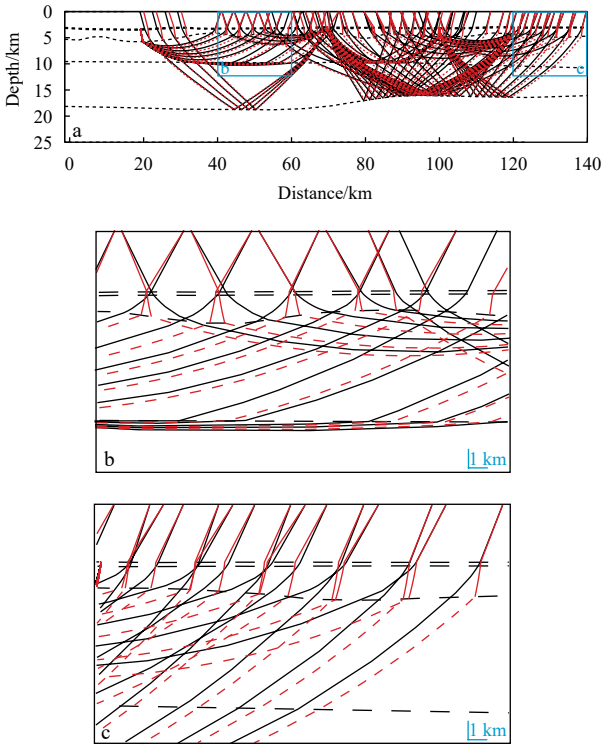

Fig. 11. Comparison of the ray paths for initial arrivals and corrected arrivals. Black solid lines represent the original ray path, and the red dotted lines represent the corrected ray path. The number of rays was reduced by 10 times.

the same inversion parameters and termination conditions. Eighty-seven inversion results were obtained with RMS and χ^2 values of 165–189 ms and 0.923–1.199, respectively. A total of 197 PSS′ and 331 PSSm′ phases were fitted to each model. Accordingly, the tomographic models were acquired (Fig. 12).

Table 2. The comparison of RMS misfit for travel time fitting of initial and corrected arrivals

Stations	Phase	Uncertainty/ ms	Initial RMS/ms	Corrected RMS/ms	ΔRMS/ ms
06	PSSc	160	198	200	2
31	PSSc	180	204	225	21
	PSSmb	180	168	174	6
37	PSSc	140	185	166	19
	PSSmb	160	165	167	2
53	PSSc	140	143	143	0
	PSSmb	180	182	195	13

The *Vs* of the crust is mainly 3.0–4.0 km/s, and the velocity contours below the model distance of 100 km also show slightly raised features, with a velocity of 3.8–3.9 km/s (Fig. 12a). The velocity standard deviation is mostly less than 0.06 km/s and increases to 0.09–0.12 km/s in local areas, indicating that the results are robust (Fig. 12b). The crustal *Vp/Vs* range from 1.70 to 1.94 (Fig. 12c), and the uppermost crust is characterized by high *Vp/Vs* (>1.80). These regions are more constrained than those in Fig. 10a because more crustal refractions were fitted. The *Vs* model shown here is similar to Fig. 10a, except for the local anomaly below the model distance of 40–60 km, where the velocity increases to 4.4 km/s and the *Vp/Vs* is of <1.7. The cause of this anomaly is analyzed in the discussion.

6 Discussion

6.1 *Influence of sedimentary layer on ray tracing*

Both forward modeling (Fig. 6d) and inversion modeling were unable to trace the near offset S-wave refractions (with an offset

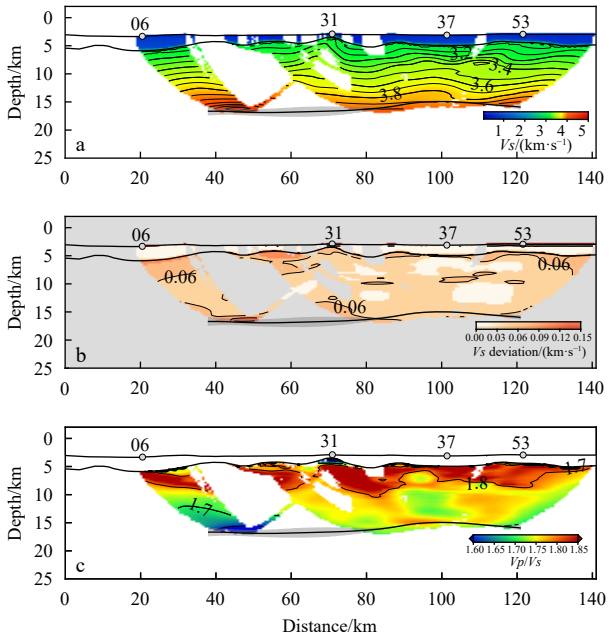

Fig. 12. The final tomographic *Vs* model based on PSS′ phases. a. The average *Vs* model. The contour interval is 0.1 km/s. b. The standard deviation of *Vs*. c. The *Vp/Vs* model was calculated from the division of the *Vp* model (Fig. 2b) by the *Vs* model (Fig. 12a). Gray areas show the Moho depth standard deviation.

of –30–30 km). Similar ray tracing phenomena were also found in previous studies of OBS2019-1 (Liu et al., 2023), NS5 (Wen et al., 2021b), OBS2016-2 (Hou et al., 2019), OBS2006-1(Wei et al., 2017), and OBS973-2 (Wei et al., 2015). Seismic ray tracing indicates that the S-wave refractions within 40 km offsets are most likely to be untraceable. Ma et al. (2021) assessed the influence of shallow structure uncertainty on forward *Vp* modeling, and the results suggested that the sedimentary layer with high velocity makes the near offset crustal refraction phases (Pg) cannot be traced. Therefore, we infer that sediment velocities may be a major factor affecting the ray tracing of the S-wave phases.

To analyze the influence of sediments on seismic rays, we conducted numerical experiments on sediment models with different velocities and thicknesses using synthetic travel time data. The ray tracing results show that the number of traced refractions decreases with increasing sediment velocities (Figs 13a–c). The number of rays decreased by 50% when the sediment velocity increased from 3.0 km/s to 3.5 km/s. The variation in sediment thickness had little impact on the rays (Figs 13d–f). Notably, the fluctuation of the sedimentary basement interface below the OBS station may cause the influence to be enhanced (Figs 13g–i). For example, if the depth node of the basement interface is modified from the model distance of 81 km to 71 km but the depth is fixed, then the right branch of the rays cannot be traced (Figs 13–i). When the depth node is adjusted to 72 km, the rays can be traced again. We thereby infer that this situation can be resolved by the fine adjustment of the model. The variation in sediment velocities and thickness has a small influence on the Moho S-wave reflections (Figs 13j–l) owing to the large incident angles of these rays. The incident angle of the Moho reflections was larger than that of the crustal refractions, with a maximum angle difference of 18° (Figs 13f and l).

We directly set the crustal velocity as the *Vs* to simulate the ray tracing of PSP′ arrivals (Figs 13m–r). The results are similar to

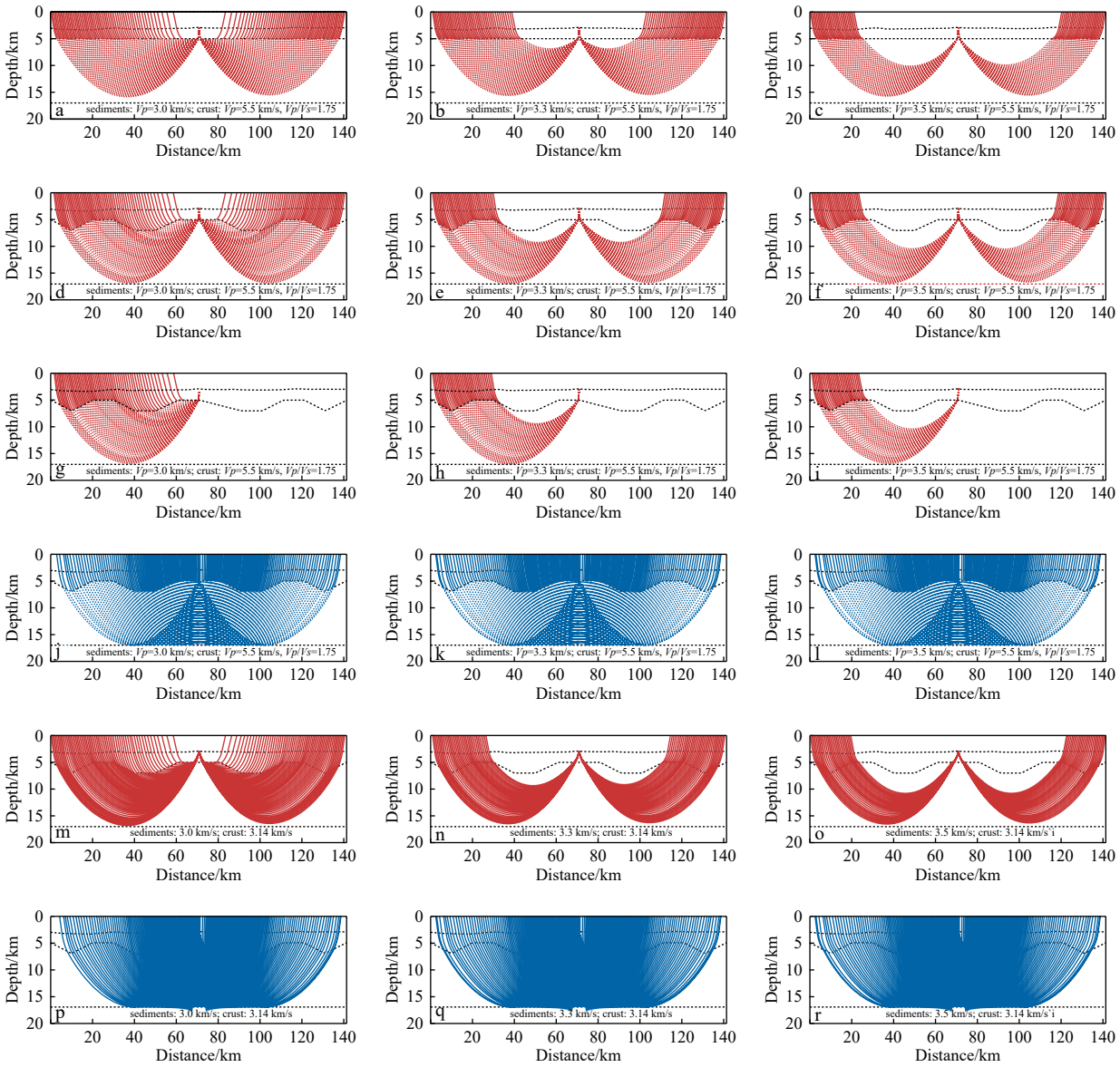

Fig. 13. Ray tracing of different sediment models based on synthetic data. The rays are converted into S-waves at the sedimentary basement in the a–l model, and the *Vp* and *Vp/Vs* of the uppermost crust are 5.5 km/s and 1.75, respectively. Solid lines represent P-wave paths; dotted lines represent S-wave paths. The velocity of the uppermost crust in the m–r model is set to 3.14 km/s (same as the *Vs* calculated by the transformation in the previous model).

those of the model with P-wave to S-wave conversion (Figs 13d–f and 13j–l), showing that the sediment velocities are an important influencing factor for the S-wave refractions (Figs 13m–o), but they have little influence on the Moho reflections (Figs 13p–r). In addition, when the sediment velocities are 3.5 km/s, the number of rays in the Fig. 13o model is reduced by approximately 12% compared with the Fig. 13f model, which coincides with the fact that more refractions are fitted in the inversion model based on PSS′ arrivals.

Additionally, we constructed 2 100 models for new seismic ray tracing based on Fig. 13m (the sedimentary basement is set as a horizontal interface with a depth of 5 km) and counted the number of fitted rays in order to objectively evaluate the influence of sediment velocities on ray tracing. The uppermost crustal *Vs* is modified in the range of 2.5–3.5 km/s, and the sediment velocity is equal to the uppermost crustal *Vs* but varies in the range of –0.1–0.1 km/s (ΔV in Fig.14). The step size of the velocities is set to 0.01 km/s, thereby 2 100 modified models are obtained. The results (Fig. 14) demonstrate that if the sediment velocities are greater than the crustal *Vs* by 0.01–0.03 km/s (ΔV= 0.01–0.03 km/s), the number of fitted rays from the new model decreases significantly (the fitting degree decreases). Higher sediment velocities result in a greater inability to trace the near offset S-wave phases. In this study, the *Vp* of the lowermost sediments is up to 3.5 km/s, which is significantly higher than the *Vs* of 3.14 km/s at the uppermost crust. The near offset seismic rays cannot propagate downward as a result. This test shows that the near offset S-wave from basement conversion cannot be traced when the lowermost sediment *Vp* is obviously higher than the uppermost crustal Vs, which may provide a reference for the S-wave modeling.

6.2 *Evaluation and comparison of the travel time correction methods*

The velocity difference (Fig. 15) between the two tomographic inversion models (Figs 10a and 12a) was obtained to evaluate the reliability of the two travel time correction methods. The characteristics of the crustal velocity field in the two models are roughly similar, with ΔVs of <0.15 km/s (mainly 0–0.1 km/s), mostly within the velocity standard deviation range of 0–0.12 km/s (Figs 10b and 12b), indicating that the two inversion results have good consistency.

We found a large velocity difference (ΔVs >0.2 km/s) in the lowermost crust below the model distance of 40–60 km. The inversion result from Method 2 most likely causes this difference; a high-velocity anomaly with a *Vs* of 4.4 km/s is imaged in the model (Fig. 12a); however, the *Vp* model does not support this anomaly (Fig. 2). The forward crustal *Vs* model (Fig. 7a) was adopted in the correction of Method 2; therefore, the influence of this model should be excluded. Consequently, we selected a random crustal model (the velocities are set to 3.0–4.0 km/s, and the Moho interface is set to the horizontal interface of 16 km) to recorrect the picked arrivals. The average time difference (Δt) between the new corrected arrivals and the initial corrected arrivals based on the forward model is between 0.008 s and 0.027s, with the majority of the time difference distributed in the range of –0.04–0.04 s (accounted for 86% of the data, Fig. 16). Consequently, the travel time correction of Method 2 did not depend on any crustal model. The forward model is recommended for the correction of Method 2 because the number of corrected arrivals increases by 26% (Fig. 16). Furthermore, we noticed that a large Moho depth standard deviation (±1 km) was revealed below the high-velocity anomaly (Fig. 2b), indicating a possible correlation; thus, we infer that Method 2 is more sensitive to the poorly constrained region in the model.

Beneath a model distance of 100–120 km, the velocity difference increases to 0.15–0.2 km/s (Fig. 15). The reason for this difference is that the inversion model from Method 2 fitted more crustal refractions and showed a higher resolution in the shallow area, resulting in a larger difference than the inversion model from Method 1, which only fitted the Moho reflections.

These two travel time correction methods have their advantages. Method 1 is simple and efficient, and the arrivals can be directly corrected using the time delay between the PPSb phase and the Pg phase. However, when the sediment had higher velocities, only a few crustal refractions were traced, and estimating the time correction in the case of complicated sedimentary structures is difficult. Thus, Method 1 was suitable for situations where the sedimentary structure is simple and the sediment velocity is low. Method 2 relies on the *RayInvr* forward sediment model to correct travel times. The correction is slightly complicated, but the result has a good constraint on the shallow crust, which is applicable in the case of complicated sedimentary structure (e.g., both Mesozoic and Cenozoic strata exist).

6.3 *Application of tomographic inversion to identify magmatic intrusions*

The intruded volcanic bodies beneath OBS31, as interpreted by Fan et al. (2019) along NS5, are also identified on the single-channel seismic profile along EW6 (Fig. 17a) because the two

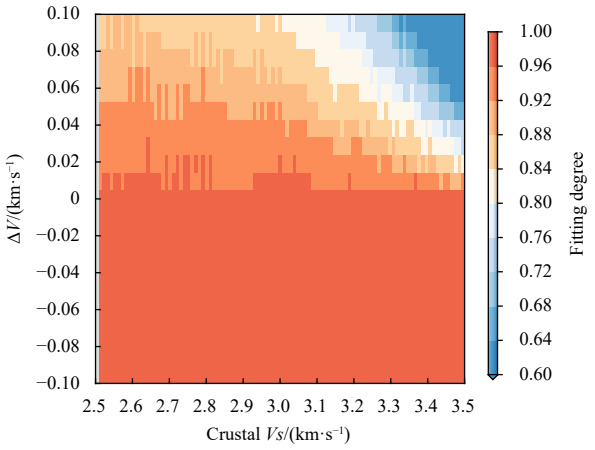

Fig. 14. Seismic ray tracing results from 2 100 models reveal the influence of sediment velocities on ray tracing. ΔV is the *Vp* of the lowermost sediments minus the *Vs* of the uppermost crust. The fitting degree is calculated by dividing the fitted phases by the picked phases.

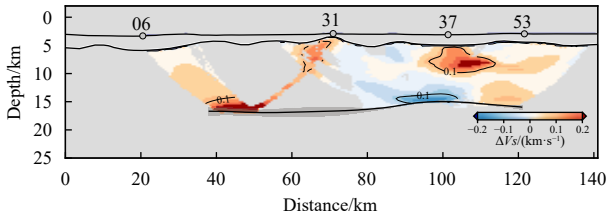

Fig. 15. Inversion results comparison of different travel time correction methods. The *Vs* difference was obtained from Fig. 12b model minus the Fig. 10b model. Gray areas show the Moho depth standard deviation.

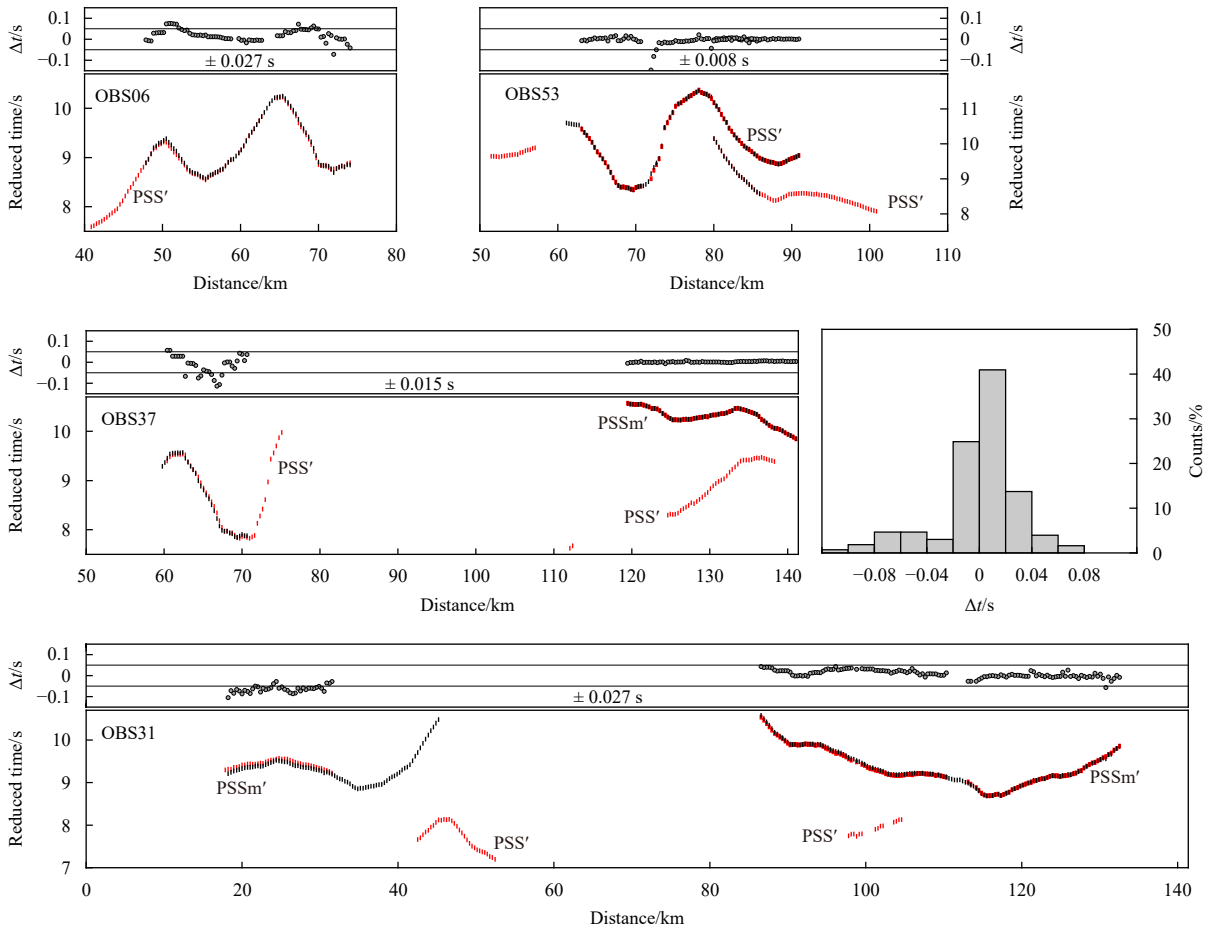

Fig. 16. Comparison of the travel time correction result based on different crustal models. The red and black dots are the travel time correction results based on the forward S-wave crustal model and random crustal model, respectively. The gray circles represent time difference between the two results, and the thin gray solid lines are the values of –0.05 s and 0.05 s. The histogram shows the distribution of the travel time difference between the two results.

seismic profiles intersect at OBS31. The upper crust below the intruded volcanic bodies is characterized by high *Vs* and *Vp*/*Vs*, according to both forward and inversion results (Figs 7, 10, and 12), however, abrupt horizontal changes are observed in the forward *Vs* and *Vp*/*Vs* models (Fig. 7). Furthermore, the forward *Vp*/*Vs* model has difficulty identifying local high *Vp*/*Vs* in the lower crust (Fig. 7b). In contrast, the inversion results have higher resolution and may image the lower crustal anomalies connected to the intruded volcanic bodies in addition to obtaining the high *Vp*/*Vs* in the upper crust (Fig. 12).

To clearly reveal the spatial relationship between the intruded volcanic bodies and crustal anomalies, the depth-time conversion of *Vs* and *Vp*/*Vs* models (Fig. 12) is conducted based on the *Vp* (Fig. 2b), which is comparable with the single-channel seismic profile (Figs 17b and c). The uplifted velocity contours and high *Vp*/*Vs* below the intruded volcanic bodies (Figs 17b and c) may indicate the presence of crustal conduits for magma upwelling. Combining the inversion *Vp*/*Vs* models of profile NS5 (Wen et al., 2021b) further supports the interpretation of the magmatic conduits (Fig. 17d). Previous studies have revealed that intensive post-rift magmatism is found on the continental slope of the northeastern SCS (Sun et al., 2020; Wan et al., 2019; Xia et al., 2018; Fan et al., 2017; Wang et al., 2006; Yan et al., 2001), which is confirmed by the forced fold in the Cenozoic strata (Fig. 17a). We proposed that the thin crust (with an average thickness of 12 km) and extensional faults caused by crustal hyperextension provide favorable conditions for the intense emplacement of post-rift magmatism.

7 Conclusions

Two travel time correction methods were applied to process the converted S-wave data of profile EW6 along the Dongsha area in the northeastern SCS. Tomographic inversion models were constructed, and the differences between the two inversion results were compared.

(1) Numerical experiments based on different sediment models were conducted based on the problems encountered during seismic ray tracing. The simulation results showed that ray tracing of crustal S-wave refractions is highly sensitive to sediment velocities. When the lowermost sediment *Vp* exceeds the uppermost crustal *Vs* by 0.01–0.03 km/s, the obvious phenomenon that the near offset crustal S-wave refractions cannot be traced appears. As the sediment velocities increased, the number of traced refractions decreased. In contrast, the Moho reflections had a large incident angle, slightly affected by the sediment velocity.

(2) The inversion models revealed that the results of the two travel time correction methods were highly accurate. The velocity difference between the two models is <0.15 km/s, mainly in the range of 0–0.1 km/s, almost within the velocity uncertainty range of the models. We further verified that the correction of

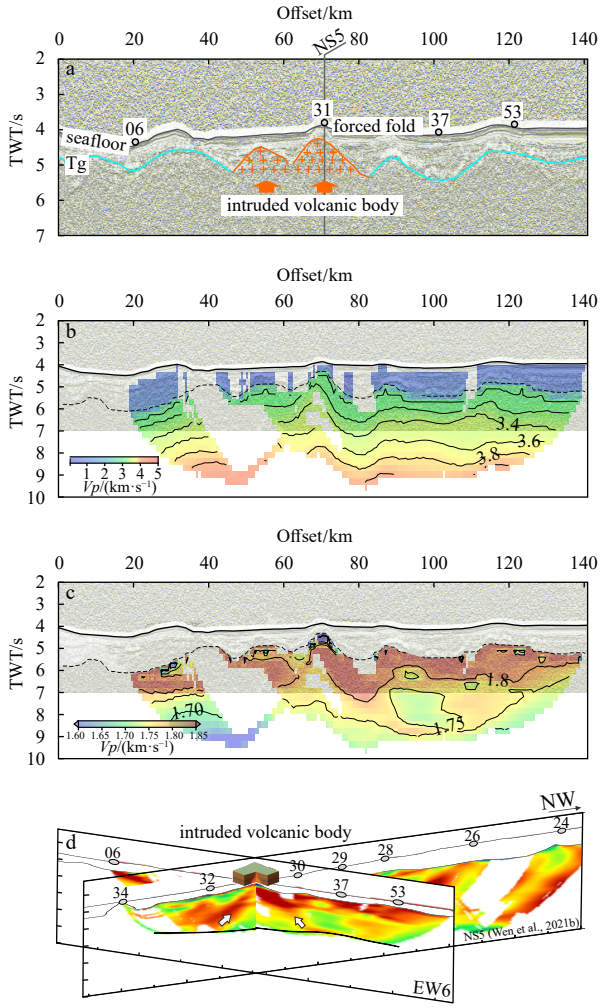

Fig. 17. The interpretation of single-channel seismic profile EW6, the intruded volcanic bodies come from Fan et al. (2019) (a). The *Vp* (b) and *Vp/Vs* (c) models for depth-to-time conversion based on the inversion *Vp* model (Fig. 2b) are superimposed on the single channel seismic profile. The black dashed line represents the *Vp* contour of 3.5 km/s. *Vp/Vs* (d) model at crossover between profile NS5 (Wen et al., 2021b) and profile EW6. TWT: two-way travel time

Method 2 allows any crustal model to correct travel times, and the results are accurate. The two travel time correction methods have their own advantages, and their applications depend on different requirements. Method 1 was used to correct the travel times when the sedimentary structure is simple and the sediment velocity is low, whereas Method 2 was more suitable for complicated sedimentary structure.

(3) The tomographic inversion method of converted S-wave provides a more objective and refined model with the ability to identify local crustal anomalies (e.g., magmatic intrusions and conduits).

Acknowledgements

The OBS data used in this study were collected onboard of RV *Shiyan 2* implementing the open research cruise NORC2014-08 supported by NSFC Shiptime Sharing Project. We are grateful to the captain, crew and scientists for their help during the cruise. The figures are plotted by Generic Mapping Tools (GMT) software (Wessel and Smith, 1998).

References

Chian D, Louden K E. 1994. The continent-ocean crustal transition across the southwest Greenland margin. Journal of Geophysical Research: Solid Earth, 99(B5): 9117–9135, doi: 10.1029/93JB03404

Christensen N I, Mooney W D. 1995. Seismic velocity structure and composition of the continental crust: a global view. Journal of Geophysical Research: Solid Earth, 100(B6): 9761–9788, doi: 10.1029/95JB00259

Christensen N I. 1996. Poisson's Ratio and crustal seismology. Journal of Geophysical Research: Solid Earth, 101(B2): 3139–3156, doi: 10.1029/95JB03446

Digranes P, Mjelde R, Kodaira S, et al. 1998. A regional shear-wave velocity model in the central Vøring Basin, N. Norway, using three-component Ocean Bottom Seismographs. Tectonophysics, 293(3–4): 157–174, doi: 10.1016/S0040-1951(98)00093-6

Du Shuyuan, Cao Jingpu, Zhou Shihong, et al. 2020. Observation and inversion of very-low-frequency seismo-acoustic fields in the South China Sea. The Journal of the Acoustical Society of America, 148(6): 3992–4001, doi: 10.1121/10.0002949

Eccles J. 2008. Shear wave analysis of volcanic rifted continental margins in the North Atlantic [dissertation]. Cambridge: University of Cambridge.

Eccles J D, White R S, Christie P A F. 2009. Identification and inversion of converted shear waves: case studies from the European North Atlantic continental margins. Geophysical Journal International, 179(1): 381–400, doi: 10.1111/j.1365-246X.2009.04290.x

Eccles J D, White R S, Christie P A F. 2011. The composition and structure of volcanic rifted continental margins in the North Atlantic: further insight from shear waves. Tectonophysics, 508(1-4): 22–33, doi: 10.1016/j.tecto.2010.02.001

Fan Chaoyan, Xia Shaohong, Cao Jinghe, et al. 2019. Lateral crustal variation and post-rift magmatism in the northeastern South China Sea determined by wide-angle seismic data. Marine Geology, 410: 70–87, doi: 10.1016/j.margeo.2018.12.007

Fan Chaoyan, Xia Shaohong, Cao Jinghe, et al. 2022. Seismic constraints on a remnant Mesozoic forearc basin in the northeastern South China Sea. Gondwana Research, 102: 77–94, doi: 10.1016/j.gr.2020.10.006

Fan Chaoyan, Xia Shaohong, Zhao Fang, et al. 2017. New insights into the magmatism in the northern margin of the South China Sea: spatial features and volume of intraplate seamounts. Geochemistry, Geophysics, Geosystems, 18(6): 2216–2239, doi: 10.1002/2016GC006792

Gao Jinwei, Wu Shiguo, McIntosh K, et al. 2015. The continent–ocean transition at the mid-northern margin of the South China Sea. Tectonophysics, 654: 1–19, doi: 10.1016/j.tecto.2015.03.003

Grevemeyer I, Hayman N W, Peirce C, et al. 2018. Episodic magmatism and serpentinized mantle exhumation at an ultraslow-spreading centre. Nature Geoscience, 11(6): 444–448, doi: 10.1038/s41561-018-0124-6

Hao Hujun, Shi Hesheng, Zhang Xiangtao, et al. 2009. Mesozoic sediments and their petroleum geology conditions in Chaoshan sag: a discussion based on drilling results from the exploratory well LF35-1-1. China Offshore Oil and Gas (in Chinese), 21(3): 151–156, doi: 10.3969/j.issn.1673-1506.2009.03.002

Hou Wenai, Li Chunfeng, Wan Xiaoli, et al. 2019. Crustal S-wave velocity structure across the northeastern South China Sea continental margin: implications for lithology and mantle exhumation. Earth and Planetary Physics, 3(4): 314–329, doi: 10.26464/epp2019033

Kodaira S, Bellenberg M, Iwasaki T, et al. 1996. V_p/V_s ratio structure of the Lofoten continental margin, northern Norway, and its geological implications. Geophysical Journal International, 124(3): 724–740, doi: 10.1111/j.1365-246X.1996.tb05634.x

Korenaga J, Holbrook W S, Kent G M, et al. 2000. Crustal structure of the Southeast Greenland margin from joint refraction and reflection seismic tomography. Journal of Geophysical Research: Solid Earth, 105(B9): 21591–21614, doi: 10.1029/2000JB900188

Lester R, Van Avendonk H J A, Mcintosh K, et al. 2014. Rifting and magmatism in the northeastern South China Sea from wide-

angle tomography and seismic reflection imaging. Journal of Geophysical Research: Solid Earth, 119(3): 2305–2323, doi: 10.1002/2013JB010639

Li Yuhan, Grevemeyer I, Huang Haibo, et al. 2021. Seismic constraint from V_p/V_s ratios on the structure and composition across the continent - ocean transition zone, South China Sea. Geophysical Research Letters, 48(16): e2021GL094656, doi: 10.1029/2021GL094656

Li Yuhan, Grevemeyer I, Huang Haibo, et al. 2022. Crustal compositional variations from continental to oceanic domain: a V_P/V_S ratio study across the zhongsha block, South China Sea. Journal of Geophysical Research: Solid Earth, 127(5): e2021JB023470, doi: 10.1029/2021JB023470

Li Zhengxiang, Li Xianhua. 2007. Formation of the 1300-km-wide intracontinental orogen and postorogenic magmatic province in Mesozoic South China: a flat-slab subduction model. Geology, 35(2): 179–182, doi: 10.1130/G23193A.1

Liu Leifeng, Xia Shaohong, Fang Yunxin, et al. 2022. Study of 1-D velocity structure of hydrate in Shenhu Area, South China Sea: based on the constraints of the hydrate zone with moderate to low saturation. Geological Journal of China Universities (in Chinese), 28(3): 424–439, doi: 10.16108/j.issn1006-7493.2021010

Liu Yutao, Li Chunfeng, Qiu Xuelin, et al. 2023. Vp/Vs ratios beneath a hyper-extended failed rift support a magma-poor continental margin in the northeastern South China Sea. Tectonophysics, 846: 229652, doi: 10.1016/j.tecto.2022.229652

Ma Fei, Huang Haibo, Qiu Xuelin, et al. 2021. Influence of shallow structure uncertainty on wide-angle seismic traveltime forward modeling-A case study using OBS2011–1 on the Xisha Block. Chinese Journal of Geophysics (in Chinese), 64(10): 3669–3684

Mjelde R. 1992. Shear waves from three-component ocean bottom seismographs off Lofoten, Norway, indicative of anisotropy in the lower crust. Geophysical Journal International, 110(2): 283–296, doi: 10.1111/j.1365-246X.1992.tb00874.x

Mjelde R, Raum T, Digranes P, et al. 2003. V_p/V_s ratio along the Vøring Margin, NE Atlantic, derived from OBS data: implications on lithology and stress field. Tectonophysics, 369(3-4): 175–197, doi: 10.1016/S0040-1951(03)00198-7

Mjelde R, Raum T, Myhren B, et al. 2005. Continent-ocean transition on the Vøring Plateau, NE Atlantic, derived from densely sampled ocean bottom seismometer data. Journal of Geophysical Research: Solid Earth, 110(B5): B05101, doi: 10.1029/2004JB003026

Nissen S S, Hayes D E, Buhl P, et al. 1995. Deep penetration seismic soundings across the northern margin of the South China Sea. Journal of Geophysical Research: Solid Earth, 100(B11): 22407–22433, doi: 10.1029/95JB01866

Qi Jianghao, Zhang Xunhua, Wu Zhiqiang, et al. 2021. Characteristics of crustal variation and extensional break-up in the Western Pacific back-arc region based on a wide-angle seismic profile. Geoscience Frontiers, 12(3): 101082, doi: 10.1016/j.gsf.2020.09.011

Qiu Xuelin, Zhao Minghui, Ao Wei, et al. 2011. OBS survey and crustal structure of the Southwest Sub-basin and Nansha Block, South China Sea. Chinese Journal of Geophysics (in Chinese), 54(12): 3117–3128, doi: 10.3969/j.issn.0001-5733.2011.12.012

Ruan Aiguo, Niu Xiongwei, Wu Zhenli, et al. 2009. The 2D velocity and density structure of the Mesozoic sediments in the Chaoshan depression. Geological Journal of China Universities (in Chinese), 15(4): 522–528

Satyavani N, Sain K, Gupta H K. 2016. Ocean bottom seismometer data modeling to infer gas hydrate saturation in Krishna-Godavari (KG) basin. Journal of Natural Gas Science and Engineering, 33: 908–917, doi: 10.1016/j.jngse.2016.06.037

Schoenberg M, Protazio J. 1992. 'Zoeppritz' rationalized and generalized to anisotropy. Journal of Seismic Exploration, 1: 125–144

Shao Lei, You Hongqing, Hao Hujun, et al. 2007. Petrology and depositional environments of mesozoic strata in the northeastern South China Sea. Geological Review (in Chinese), 53(2): 164–169, doi: 10.3321/j.issn:0371-5736.2007.02.003

Shi Hesheng, Li Chunfeng. 2012. Mesozoic and early Cenozoic tectonic convergence-to-rifting transition prior to opening of the South China Sea. International Geology Review, 54(15): 1801–1828, doi: 10.1080/00206814.2012.677136

Sibuet J C, Yeh Y C, Lee C S. 2016. Geodynamics of the South China Sea. Tectonophysics, 692: 98–119, doi: 10.1016/j.tecto.2016.02.022

Singhroha S, Chand S, Bünz S. 2019. Constraints on gas hydrate distribution and morphology in vestnesa ridge, western svalbard margin, using multicomponent ocean - bottom seismic data. Journal of Geophysical Research: Solid Earth, 124(5): 4343–4364, doi: 10.1029/2018JB016574

Sun Qiliang, Alves T M, Zhao Minghui, et al. 2020. Post-rift magmatism on the northern South China Sea margin. GSA Bulletin, 132(11-12): 2382–2396, doi: 10.1130/B35471.1

Wan Xiaoli, Li Chunfeng, Zhao Minghui, et al. 2019. Seismic velocity structure of the magnetic quiet zone and continent - ocean boundary in the northeastern South China Sea. Journal of Geophysical Research: Solid Earth, 124(11): 11866–11899, doi: 10.1029/2019JB017785

Wan Kuiyuan, Xia Shaohong, Cao Jinghe, et al. 2017. Deep seismic structure of the northeastern South China Sea: origin of a high-velocity layer in the lower crust. Journal of Geophysical Research: Solid Earth, 122(4): 2831–2858, doi: 10.1002/2016JB013481

Wang T K, Chen Mingkai, Lee C S, et al. 2006. Seismic imaging of the transitional crust across the northeastern margin of the South China Sea. Tectonophysics, 412(3–4): 237–254, doi: 10.1016/j.tecto.2005.10.039

Wang Yuan, You Qingyu, Hao Tianyao. 2022. Estimating the shear-wave velocities of shallow sediments in the Yellow Sea using ocean-bottom-seismometer multicomponent scholte-wave data. Frontiers in Earth Science, 10: 812744, doi: 10.3389/feart.2022.812744

Wei Xiaodong, Ruan Aiguo, Li Jiabiao, et al. 2017. *S*-wave velocity structure and tectonic implications of the northwestern subbasin and Macclesfield of the South China Sea. Marine Geophysical Research, 38(1–2): 125–136, doi: 10.1007/s11001-016-9288-x

Wei Xiaodong, Ruan Aiguo, Zhao Minghui, et al. 2015. Shear wave velocity structure of Reed Bank, southern continental margin of the South China Sea. Tectonophysics, 644–645: 151–160, doi: 10.1016/j.tecto.2015.01.006

Wei Xiaodong, Zhao Minghui, Ruan Aiguo, et al. 2011. Crustal structure of shear waves and its tectonic significance in the mid-northern continental margin of the South China Sea. Chinese Journal of Geophysics (in Chinese), 54(12): 3150–3160, doi: 10.3969/j.issn.0001-5733.2011.12.015

Wen Genggeng, Wan Kuiyuan, Xia Shaohong, et al. 2021a. Traveltime inversion method of converted shear waves using rayinvr algorithm. Applied Sciences, 11(8): 3571, doi: 10.3390/app11083571

Wen Genggeng, Wan Kuiyuan, Xia Shaohong, et al. 2021b. Crustal extension and magmatism along the northeastern margin of the South China Sea: further insights from shear waves. Tectonophysics, 817: 229073, doi: 10.1016/j.tecto.2021.229073

Wessel P, Smith W H F. 1998. New, improved version of generic mapping tools released. Eos, Transactions American Geophysical Union, 79(47): 579,doi: 10.1029/98EO00426

Xia Shaohong, Cao Jinghe, Wan Kuiyuan, et al. 2016. Role of the wide-angle OBS seismic exploration in the research of marine sedimentary basin. Advances in Earth Science (in Chinese), 31(11): 1111–1124, doi: 10.11867/j.issn.1001-8166.2016.11.1111

Xia Shaohong, Qiu Xuelin, Zhao Minghui, et al. 2007. Data processing of onshore-offshore seismic experiment in Hongkong and Zhujiang River Delta region. Journal of Tropical Oceanography (in Chinese), 26(1): 35–38

Xia Shaohong, Zhao Fang, Zhao Dapeng, et al. 2018. Crustal plumbing system of post-rift magmatism in the northern margin of South China Sea: new insights from integrated seismology. Tectonophysics, 744: 227–238, doi: 10.1016/j.tecto.2018.07.002

Yan Pin, Wang Liaoliang, Wang Yanlin. 2014. Late Mesozoic compressional folds in Dongsha Waters, the northern margin of the South China Sea. Tectonophysics, 615–616: 213–223,doi: 10.1016/j.tecto.2014.01.009

Yan Pin, Zhou Di, Liu Zhaoshu. 2001. A crustal structure profile across the northern continental margin of the South China Sea. Tectonophysics, 338(1): 1–21, doi: 10.1016/S0040-1951(01)00062-2

Yang Shengxiong, Qiu Yan, Zhu Benduo, et al. 2015. Atlas of Geology and Geophysics of the South China Sea (in Chinese). Tianjin: China Navigation Publications.

Zelt C A, Smith R B. 1992. Seismic traveltime inversion for 2-D crustal velocity structure. Geophysical Journal International, 108(1): 16–34, doi: 10.1111/j.1365-246X.1992.tb00836.x

Zhang Jie, Li Jiabiao, Ruan Aiguo, et al. 2018. Application of converted S-waves from the active-source ocean bottom seismometer experiment. Earth Science (in Chinese), 43(10): 3778–3791

Zhang Haoyu, Qiu Xuelin, Huang Haibo, et al. 2022. CALM: a software tool for rapid analysis and modeling of converted shear waves in wide-angle seismic data. Computers & Geosciences, 166: 105163, doi: 10.1016/j.cageo.2022.105163

Zhang Li, Zhao Minghui, Qiu Xulin, et al. 2016. Recent progress of converted shear-wave phase identification in Nansha Block using ocean bottom seismometers data. Journal of Tropical Oceanography (in Chinese), 35(1): 61–71, doi: 10.11978/2015025

Zhao Minghui, Qiu Xuelin, Xia Kanyuan, et al. 2004. Onshore-offshore seismic data processing and preliminary results in NE South China Sea. Journal of Tropical Oceanography (in Chinese), 23(1): 58–63

Zhao Minghui, Qiu Xuelin, Xia Shaohong, et al. 2007. Identification and analysis of shear waves recorded by three-component OBSs in northeastern South China Sea. Progress in Natural Science (in Chinese), 17(11): 1516–1523.

Zhao Minghui, Qiu Xuelin, Xia Shaohong, et al. 2010. Seismic structure in the northeastern South China Sea: S-wave velocity and Vp/Vs ratios derived from three-component OBS data. Tectonophysics, 480(1-4): 183–197, doi: 10.1016/j.tecto.2009.10.004

Zhao Weina, Wu Zhiqiang, Hou Fanghui, et al. 2023. Velocity structure in the South Yellow Sea basin based on first-arrival tomography of wide-angle seismic data and its geological implications. Acta Oceanologica Sinica, 42(2): 104–119, doi: 10.1007/s13131-022-2028-y